Nickel boride (Ni_xB) as a highly efficient catalyst for oxygen evolution

Justus Masa[a*], Ilya Sinev[b], Hemma Mistry[b,c], Edgar Ventosa[a], Maria de la Mata[e], Jordi Arbiol[e,f], Martin Muhler[d], Beatriz Roldan Cuenya[b], Wolfgang Schuhmann[a*]

[a] Analytical Chemistry - Center for Electrochemical Sciences (CES), Ruhr-Universität Bochum, Universitätsstr. 150, D-44780 Bochum (Germany)

[b] Department of Physics, Ruhr-Universität Bochum, Universitätsstr. 150, D-44780 Bochum (Germany)

[c] Department of Physics, University of Central Florida, Orlando, FL 32816, USA

[d] Laboratory of Industrial Chemistry, Ruhr-Universität Bochum, Universitätsstr. 150, D-44780 Bochum (Germany)

[e] Catalan Institute of Nanoscience and Nanotechnology (ICN2), CSIC, and The Barcelona Institute of Science and Technology (BIST), Campus UAB, Bellaterra, 08193 Barcelona, Catalonia, Spain

f ICREA, Pg. Lluís Companys 23, 08010 Barcelona, Catalonia, Spain

* Correspondence should be addressed to: justus.masa@rub.de and wolfgang.schuhmann@rub.de

Abstract

The overriding obstacle to mass hydrogen production as the premium fuel for powering our planet is the frustratingly slow kinetics of the oxygen evolution reaction (OER). Additionally, inadequate understanding of the key barriers of the OER is a hindrance to insightful design of advanced OER catalysts. Herein, we present amorphous nickel boride (Ni_xB) as a low-cost, very efficient and stable catalyst for the OER during electrochemical water splitting. The catalyst afforded 10 mA cm^{-2} at 0.38 V overpotential during OER in 1.0 M KOH, which reduced to only 0.28 V at 20 mA cm^{-2} when supported on nickel foam. *Operando* XAFS measurements revealed prevalence of NiOOH, as well as Ni-B under OER conditions, owing to a Ni-B core@nickel oxyhydroxide shell (Ni-B@NiO_xH) structure, and increase in disorder of the NiO_xH layer, thus unveiling important insight into the transient states of the catalyst during oxygen evolution.

Keywords: Nickel boride, water oxidation, water splitting, hydrogen evolution, oxygen evolution, XAFS

Electrochemical water splitting for hydrogen production is impeded by intensive energy consumption mostly due to the slow kinetics of the oxygen evolution reaction (OER), and the requirement to use costly and rare platinum group metal (PGM) catalysts, rendering the process of low economic appeal[1,2]. Efforts to reduce or completely substitute the use of PGM electrocatalysts (Pt, IrO_2 and RuO_2), the state-of-the catalysts for electrochemical water splitting (ECWS), with less costly alternatives to leverage the competitiveness of ECWS have been futile in the past[1]. Moreover, even with Pt as the cathode, and RuO_2 or IrO_2 as the anode, large overpotentials are still incurred to achieve meaningful electrolysis rates[3,4]. ECWS using non-precious metal catalysts is more promising in high pH electrolytes, where Ni, Co and Fe-based materials are very promising[5,6]. Specifically, mixed metal oxides and hydroxides with a layered structure[7–11], and compounds of Co and Ni incorporating non-metal elements, typically, B, N, S, Se and P, have proved phenomenal in alkaline water oxidation, with activities surpassing RuO_2 and IrO_2 being reported for NiSe[5], Ni_5P_4[6], Ni_2P[7], CoP[8,12], Ni_3N[9,10], among others. Meanwhile, binary and ternary compounds of Co, Fe, Mo, W, and Ni with B, P, S, and Se, among others, also exhibit outstanding activity in catalyzing the hydrogen evolution reaction (HER)[13–18]. These developments inspire new directions in the search for advanced non-precious catalysts for ECWS.

Herein, we show that nickel boride (Ni_xB) is a remarkably active and stable non-precious metal catalyst for oxygen evolution under alkaline conditions. The catalyst afforded 10 mA cm^{-2} at 0.38 V overpotential during OER in 1.0 M KOH, which reduced to only 0.28 V at 20 mA cm^{-2} when supported on nickel foam. Additionally, we present insight from *operando* XAFS of the nature of transient states of the catalyst during oxygen evolution. The active form of the catalyst is a Ni-B@NiOOH (core@shell) structure. We observed a contraction of the Ni-O bonds in NiOOH accompanied with increase in disorder of the layer during active oxygen evolution.

Catalyst preparation and characterization

Nickel boride (Ni_xB) was prepared by chemical reduction of nickel ions in a deaerated 1.0 M $NiCl_2$*6 $H_2O_{(aq)}$ solution using 1.0 M $NaBH_{4(aq)}$ (see SI for details). The composition of Ni and B in the product was 76.2 % and 6.6 % respectively, corresponding to a Ni:B stoichiometry of 2:1 (Table S1), the rest being mostly oxygen (Fig. S1). X-ray diffraction (XRD) studies (Fig. 1) revealed Ni_xB to be XRD amorphous. The product remains XRD amorphous upon annealing

under Ar at 300 °C for 2 h. Further increase of the annealing temperature to 600°C led to crystallization and emergence of Ni_3B (ICSD: 614985) as the major phase, and Ni_2B (ICSD 75792) as a minor phase. Ni_3B remained the dominant phase in the sample annealed at 1000 °C, with minor reflections assignable to Ni_2B also detectable. Structure refinement using Rietveld analysis revealed that Ni_xB-1000 contained 79% Ni_3B while Ni_2B made up 21%. Ni_xB annealed at 300 °C (Ni_xB-300) exhibited the best electrochemical performance (discussed later) and was thus characterized in more detail.

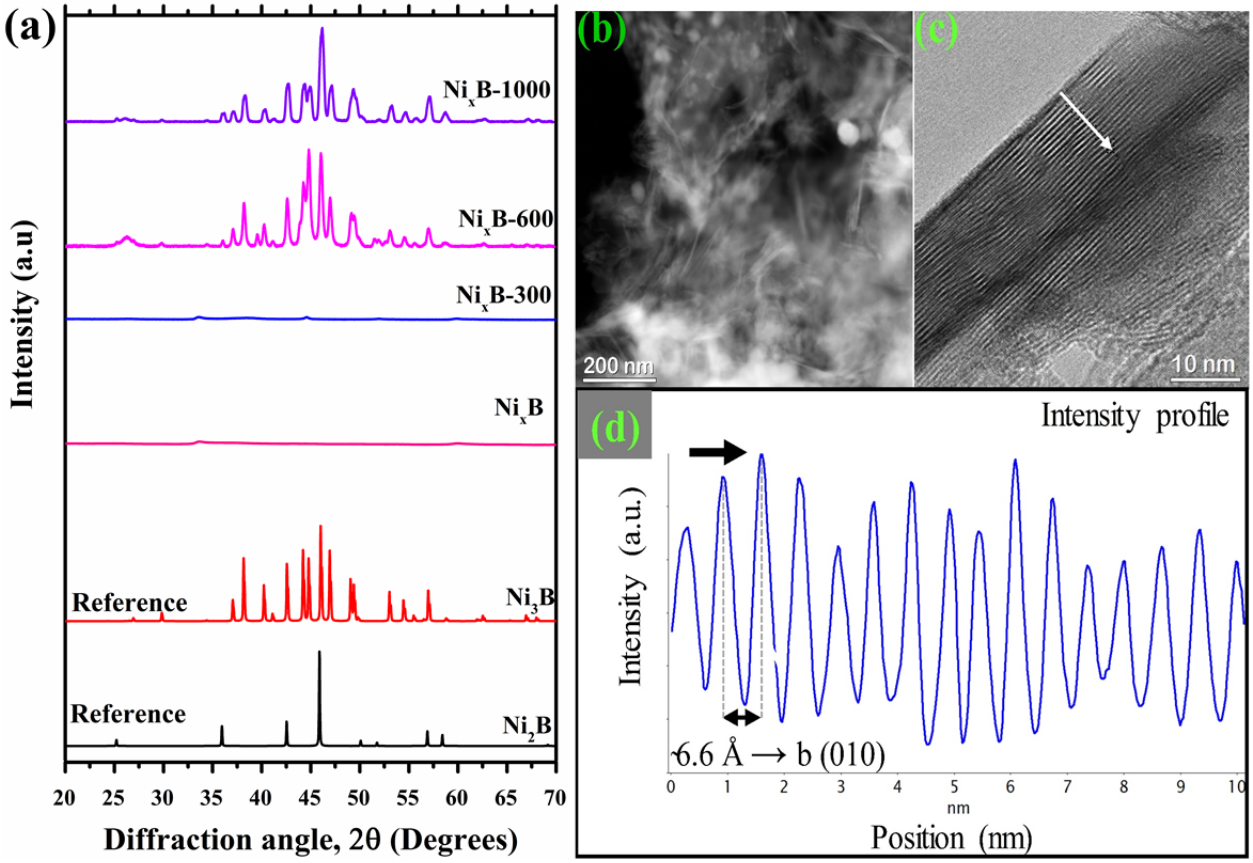

Figure 1| (a) XRD pattern of Ni_xB, Ni_xB annealed at 300 °C (Ni_xB-300), 600 °C (Ni_xB-600), and at 1000 °C (Ni_xB-1000), and of the references Ni_2B (ICSD 75792) and Ni_3B (ICSD 614985). (b) High-angle annular dark field (HAADF) low magnification TEM micrograph of Ni_xB-300, (c) HRTEM of a single particle showing layers of sheets, (d) intensity profile taken across the flake along the white arrow in (c) showing individual sheets with a thickness of ≈ 6.6 Å.

Ni_xB-300 comprised of very thin sheets as well as discrete particles (Fig. 1b). High resolution TEM (HRTEM) analysis of an individual flake of Ni_xB-300 (Fig. 1c) reveals atomically thin layers with a thickness of about 6.6 Å (Fig. 1d). Spectroscopic analysis by

electron energy loss spectroscopy (EELS) shows that the discrete particles are predominantly nickel boride, while the sheets have a uniform distribution of Ni, B, as well as oxygen (Fig. S3). Fast Fourier Transform (FFT) analysis of selected regions of the HRTEM images disclosed predominance of Ni_2B nanocrystallites in Ni_xB-300 (Fig. S4). Crystallites of Ni_3B were also occasionally found (Fig. S5). In consideration of the XRD and TEM observations, it can be concluded that Ni_xB-300 was composed of nanocrystallites of Ni_2B, and Ni_3B to a less extent, as well as very small particles of $Ni^{(0)}$. The predominance of the Ni_3B phase at high annealing temperatures, as confirmed by XRD, indicates thermally induced phase transition of Ni_2B to Ni_3B, and also suggests the reaction of Ni with Ni_2B to form Ni_3B ($Ni + Ni_2B \rightarrow Ni_3B$), consistent with the work by Glavee et al.[19,20] among others.

XPS and XAFS characterization

XPS examination of the chemical state of as prepared Ni_xB minimally exposed to air showed the main Ni $2p_{3/2}$ and Ni $2p_{1/2}$ core peaks at 852.5 eV and 869.6 eV (Fig. 2a(i)), respectively, typical of Ni_2B[21]. The Ni $2p_{3/2}$ and Ni $2p_{1/2}$ satellite peaks at 855.6 eV and 873.0 eV, respectively, are due to Ni^{2+}, indicating the presence of surface oxide or hydroxide species. Amorphous metal borides are spontaneously oxidized when exposed to air and water to form surface oxides/hydroxides leading to a core@shell (metal boride@metal oxide/hydroxide) structure[22–24]. Ni_xB exposed to air, (Fig. 2a(ii), thus exhibited a predominantly oxidized surface with a dominant Ni $2p_{3/2}$ peak at 855.82 eV (Ni^{2+} species) and minor peak at 852.52 eV due to the interaction of nickel with boron (Fig. 2a). A positive chemical shift of 0.95 eV in the binding energy of the Ni $2p_{3/2}$ peak was observed upon annealing Ni_xB at 300 ^oC (Fig 2c), indicating relative displacement of electrons from nickel. The annealing process thus led to modification of the surface electronic structure of Ni_xB-300, which had a beneficial effect on its OER activity.

The B 1s spectrum of as prepared Ni_xB minimally exposed to air (Ni_xB-(i) in Fig 2b) was deconvoluted into two distinct species at 187.9 eV and 191.8 eV (Fig. 2b). The species at 187.9 eV is due to interaction of boron with nickel, whereas the one at 191.8 eV is due to boron-oxo species. On the other hand, the B 1s spectrum of Ni_xB exposed to air for several hours (Ni_xB-(ii) in Fig 2b) was deconvoluted into two contributions at 190.07 eV and 192.0 eV both corresponding to boron oxide species. The O 1s spectrum of Ni_xB-300 (Fig 2d), not activated sample, shows that its surface was covered with $Ni(OH)_2$. Meanwhile, after electrochemical

activation (activated in Fig 2d), which involved 50 cycles of potential cycling in 1.0 KOH between 0.95 V and 1.65 V vs RHE, the surface was mainly covered with a nickel oxyhydroxide (NiOOH) layer.

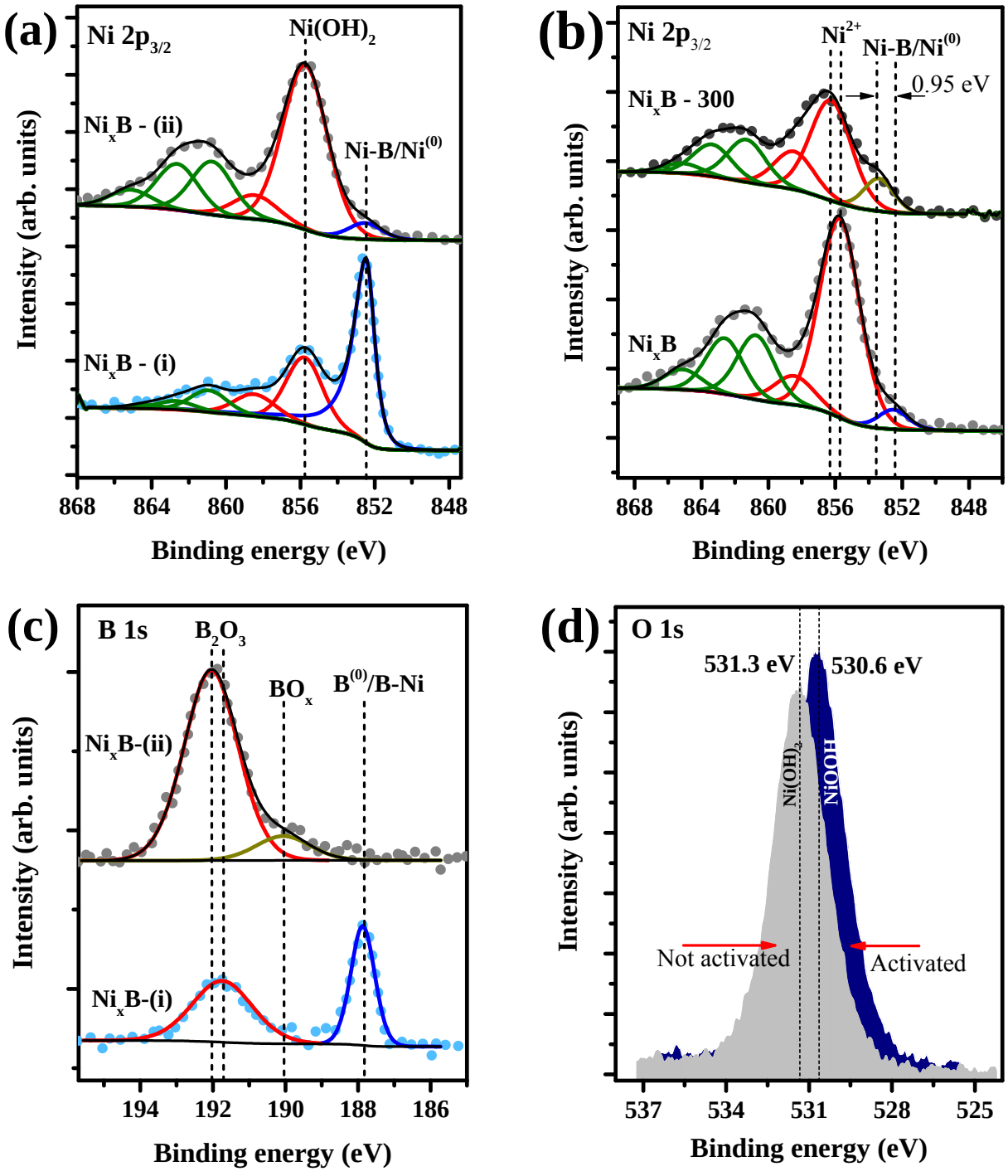

Figure 2| XPS analysis: (a) Ni 2p (a) and (b) B 1s core-level spectra of Ni_xB minimally exposed to air (i) and after prolonged air exposure (ii). (c) Ni 2p core-level spectra of Ni_xB and Ni_xB after

annealing under argon at 300 °C, and (d) O 1s high-resolution spectra of Ni_xB-300 before and after electrochemical activation.

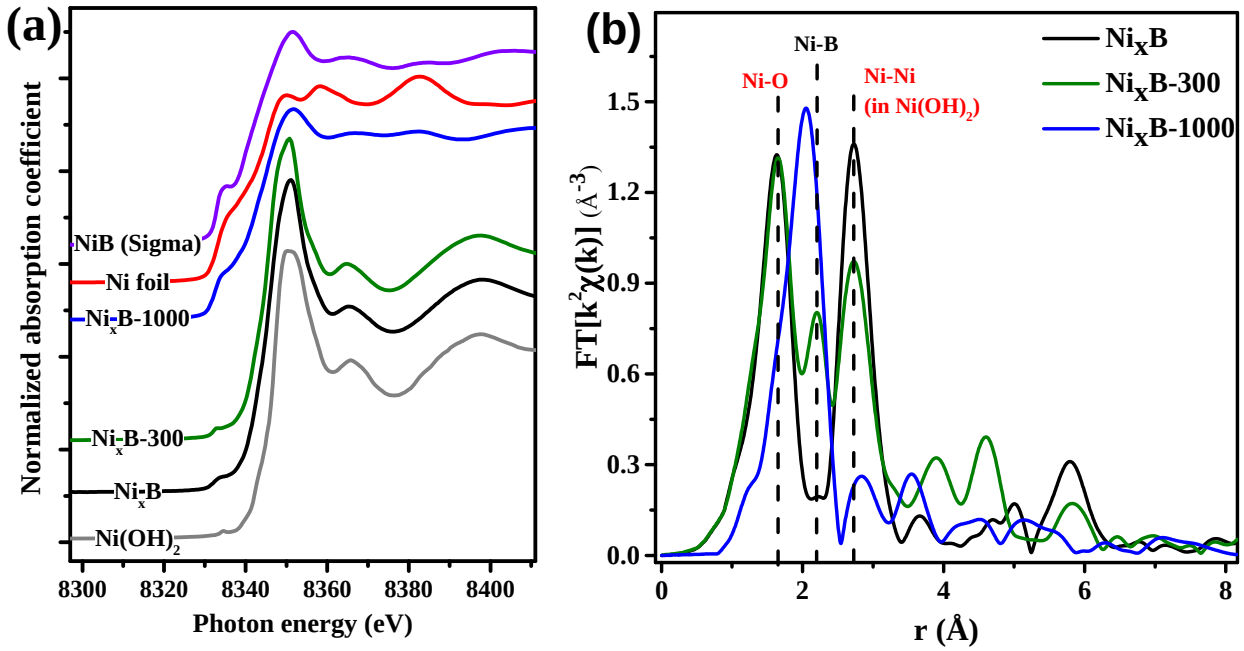

Figure 3 | (a) X-ray absorption near-edge structure (XANES) spectra of the as prepared Ni_xB sample, Ni_xB annealed at 300 °C (Ni_xB-300) under argon, Ni_xB annealed at 1000 °C under argon (Ni_xB-1000), a Ni-foil, NiB (Sigma Aldrich) and $Ni(OH)_2$ as references. (b) Extended X-ray absorption fine structure (EXAFS) spectra of Ni_xB, Ni_xB-300, and Ni_xB-1000.

X-ray absorption fine-structure spectroscopy (XAFS) measurements were carried out on Ni_xB, Ni_xB-300 and Ni_xB-1000 to probe the influence of annealing temperature on the chemical state and local coordination structure of the catalyst. X-ray absorption near edge structure (XANES) spectra are presented in Figure 3(a). The pre-edge region of Ni_xB and Ni_xB-300 consist of a small peak at ca. 8327.2 eV whose shape and position match very well with $Ni(OH)_2$ and NiO (not shown) reference spectra. The first feature above the absorption edge (white-line) centred at 8344.6 eV, is also in agreement with the NiO and $Ni(OH)_2$ spectra, thus indicating predominance of the Ni^{2+} state in the samples. On the other hand, the XANES spectrum of Ni_xB-1000 shows close resemblance to a commercial nickel boride reference (Sigma Aldrich), featured by a white line significantly less intense than the Ni^{2+} references. In this case, the XANES results are in good agreement with XRD data described before. However, the reference

nickel boride sample, NiB (Sigma-Aldrich) was composed of several distinct Ni_xB_y phases and was thus not a suitable reference for discussion of the EXAFS data following hereafter.

Extended X-ray absorption fine-structure (EXAFS) spectra of Ni_xB, Ni_xB-300 and Ni_xB-1000 (Fig. 3b) reveal significant differences induced by the annealing processes on the local environment of nickel. The shape of both Ni_xB and Ni_xB-300 spectra show the presence of backscattering events characteristic of Ni^{2+} compounds, namely Ni-O at 2.07 Å and Ni-Ni at 3.1 Å (uncorrected for phase shift). There is an extra peak emerging at 2.2 Å (uncorrected) on the EXAFS spectrum of the sample annealed at 300°C indicating the presence of B in a local Ni environment. Moreover, peak separation of the spectrum for the untreated Ni_xB sample with a plateau between 2.1 and 2.3 Å gives hint of a similar Ni-B coordination. Detailed analysis of the EXAFS spectra performed by fitting a combination of Ni-O, Ni-B and Ni-Ni^{2+} backscattering paths to the spectral features described above, gives proof to the hypothesis of the presence of boron as nearest neighbour in Ni local coordination (see Table S2 for details). Thus, in the as prepared Ni_xB sample, the effective Ni-B coordination number is as low as 1.8, while a high value of the corresponding σ^2 ($11.9 \cdot 10^{-3}$ Å^2) indicates significant disorder in the boride structure. Annealing at 300 °C results in an increase of the Ni-B coordination number to 4.2, and ordering of the boride structure with a less ordered $Ni(OH)_2$ phase evidenced by a lower Ni-Ni^{2+} coordination number and higher σ^2. The EXAFS spectrum of Ni_xB-1000 is dominated by a peak at 2.05 Å (uncorrected), and can be fitted for the most by Ni-B and a minor amount of Ni-O. The Ni-B coordination number as high as 13.4 in this case can be interpreted by overlapping of several Ni-B backscattering events from different well-ordered Ni_xB_y phases, as indicated by XRD.

Electrocatalysis of the oxygen evolution reaction (OER)

A film of Ni_xB was adsorbed on a glassy carbon electrode and investigated for electrocatalysis of OER in 0.1 M KOH (see SI for details of film preparation). Before acquiring any electrochemical data, the electrode was first subjected to continuous potential cycling at a scan rate of 0.1 V s^{-1} between 0.95 to 1.65 V (RHE) until reproducible voltammograms were obtained (Fig. 3a). The continuous increase in the intensity of both the anodic and cathodic peaks centred at about 1.40 V is due to growth of a NiOOH layer (Fig. 2d). The anodic process is due

to oxidation of Ni^{2+} to Ni^{3+}, while the reverse process is the reduction of Ni^{3+} back to Ni^{2+}, that is, $Ni(OH)_2 + OH^- \leftrightarrow NiOOH + H_2O + e^-$. Results for OER electrocatalysis by Ni_xB in 0.1 M KOH are presented in Fig. 3b. The OER activity of Ni_xB became enhanced upon annealing in argon for 2 hours, reaching a maximum at 300 ^oC followed by a drastic decline at higher annealing temperatures. The catalyst was not able to attain 10 mA cm^{-2} within the investigated potential window (1.0 - 1.8 V) when annealed at or above 700 ^oC. The inset of Fig. 3b shows variation of the OER activity of Ni_xB with annealing temperature, expressed as the potential corresponding to a current density of 10 mA cm^{-2}. The non-annealed sample, Ni_xB, attained 10 mA cm^{-2} at 1.73 V, while Ni_xB-200 and Ni_xB-300 afforded 1.68 and 1.61 V, respectively, at the same current density. Importantly, Ni_xB-300 exhibited better OER activity than Ni_xB-200 despite the former possessing a slightly lower BET surface area, 122.3 m^2 g^{-1} for Ni_xB-300 versus 127.4 m^2 g^{-1} for Ni_xB-200 (Table S1). This implies that increase of the OER activity from Ni_xB through Ni_xB-200 and Ni_xB-300, cannot be explained in terms of surface area.

It is worth to note that the intensity of the $Ni^{2+} \leftrightarrow Ni^{3+}$ redox peaks followed a trend exactly similar to the OER activity dependence on temperature. Characteristically, the area under the $Ni^{2+} \leftrightarrow Ni^{3+}$ redox peaks is proportional to the amount of electrochemically addressable nickel atoms/ions, which is intimately linked to conductivity. The observed enhancement of the OER activity with annealing temperature is thus mainly attributed to an increase of the electrical conductivity of the catalyst due to sintering of the catalyst particles. Besides affecting the geometrical properties, XPS analysis revealed that the annealing process also induces changes in the chemical state of the catalyst surface ascribed to electronic structure modification. For example, a positive chemical shift in the BE of the Ni 2p3/2 peak of 0.95 eV, from 852.4 eV to 853.5 eV, was observed when Ni_xB was annealed at 300 ^oC (Fig. 2c). The decline in activity at much higher annealing temperatures is certainly due to decrease of the surface area due to the growth in particle size. The BET surface area decreased from 122.3 m^2 g^{-1} for Ni_xB-300 to 16.3 m^2 g^{-1} for Ni_xB-600, and to 7.9 m^2 g^{-1} for Ni_xB-1000.

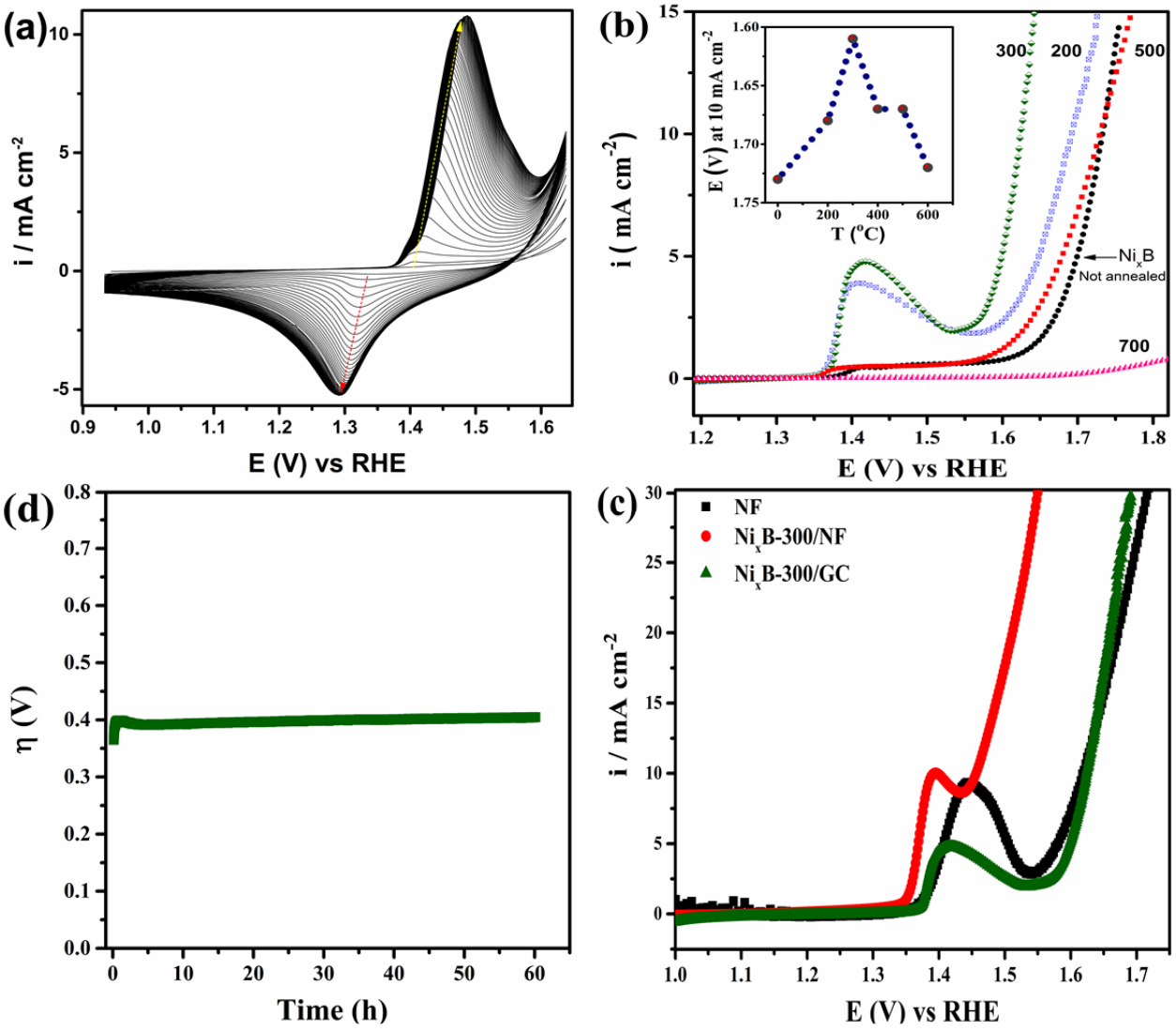

Figure 4 | (a) Activation of Ni_xB by continuous potential cycling between 0.95 V and 1.65 V at 100 mV s^{-1} in 0.1 M KOH; (b) Linear sweep voltammograms (LSVs), corrected for the resistance of the electrolyte, of Ni_xB and Ni_xB annealed at 200 °C, 300 °C, 500 °C and 700 °C, recorded at 10 mV s^{-1} in 0.1 M KOH and at 1600 rpm electrode rotation. Inset: variation of the OER activity of Ni_xB, expressed as the potential at a current density of 10 mA cm^{-2}, with annealing temperature. (c) Galvanostatic long-term stability measurement of Ni_xB-300 deposited on a graphite rotating disk electrode (area = 0.196 cm^2) at 10 mA cm^{-2} in KOH (0.1 M); (d) comparative LSVs of a bare nickel foam (NF) electrode, and Ni_xB-300 supported on glassy carbon (Ni_xB-300/GC) and on nickel foam (Ni_xB@NF).

Galvanostatic long-term stability measurements of Ni_xB-300 supported on a graphite RDE electrode at a current density of 10 mA cm^{-2} in 0.1 M KOH indicate very stable performance of the catalyst with essentially no loss in performance after 60 h (Fig. 4c). In metal borides, the boron atoms are capable of forming linear, planar and three-dimensional structures surrounded by metals,[9,25] through the formation of covalent M-B, as well as B-B bonds, making these compounds extremely hard and chemically resistant.

Nickel foam is an attractive 3D catalyst support for gas evolution electrodes owing to its high surface area, stability and synergistic catalytic effect.[9,26,26–31] We supported Ni_xB-300 on nickel foam (Ni_xB-300/NF) and investigated the resulting electrodes for the OER in a custom-built flow-through cell[32]. Figure 5a shows the OER performance of the Ni_xB-300/NF electrode in 0.1 M KOH compared to Ni_xB-300 supported on glassy carbon (Ni_xB-300/GC), and bare NF. Employing NF as a support led to tremendous increase of the current and significant reduction of the overpotential. In our case, it was not valid anymore to extract the potential corresponding to a current density of 10 mA cm^{-2} since this overlapped with the gigantic $Ni^{2+} \rightarrow Ni^{3+} + e^-$ oxidation wave. A current density of 20 mA cm^{-2} (normalized to geometric electrode area) was attained at an overpotential of only 0.28 V. To benchmark the performance of Ni_xB-300, its activity was compared against some recently reported highly active non-precious OER catalysts, particularly, nickel based catalysts supported on nickel foam (Table S3). As an example, a NiFe double layer hydroxide doped with nitrogen (N-NiFe-LDH) directly grown on nickel foam, one of the best OER catalysts, afforded 0.23 V overpotential at a current density of 10 mA cm^{-2} in 0.1 M KOH [33]. The performance of Ni_xB-300 is thus clearly very promising and among the best reported for nickel based catalysts.

Operando XAFS studies

The chemical state and structure of the catalyst under OER conditions was probed via *operando* XAFS studies. Figure 5 presents overlaid *operando* XANES (a) and EXAFS (b) spectra of Ni_xB-300 after electrochemical conditioning between 1.0 V and 1.6 V, during polarization at 1.0 V, a potential below the redox transition from Ni^{2+} ($Ni(OH)_2$) to Ni^{3+} (NiOOH), and at 1.7 V, a potential at which oxygen evolution takes place. The XANES spectra of the pre-conditioned sample and during the polarization at 1.0 V do not show any differences compared to the initial state. Under OER conditions, the Ni-K edge position remains unchanged

as well, although there are clear changes in both the slope and specific features of the spectrum. The spectrum measured at 1.7 V has a lower white line intensity with its maximum shifted to higher energy. It resembles the spectrum of NiOOH, produced by *in-situ* electrochemical oxidation of $Ni(OH)_2$ at 1.6 V_{RHE} and is also similar to the spectra of Ni^{3+} species reported in the literature[34,35]. This change observed under reaction conditions indicates that there was a change in the oxidation state from Ni^{2+} to Ni^{3+} (NiOOH) taking place under OER conditions[34,35].

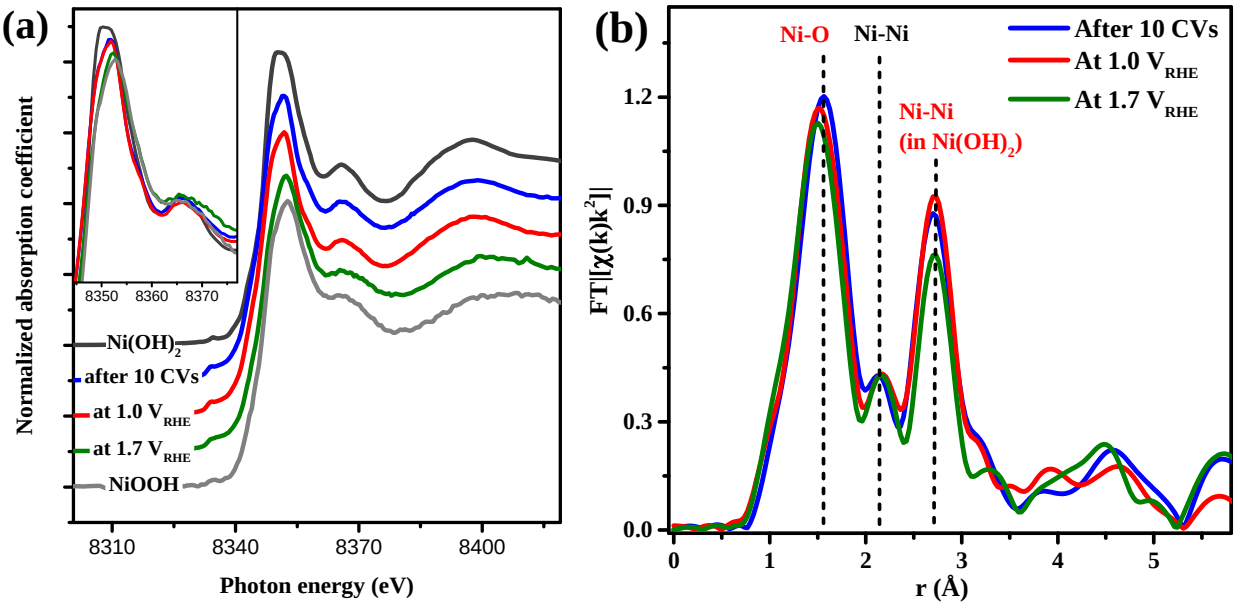

Figure 5 | *Operando* XANES (a) and EXAFS (b) spectra of Ni_xB-300 acquired after conditioning (10 CVs) during OER at different electrochemical potentials, 1.0 V and 1.7 V versus RHE.

The EXAFS spectra measured under *operando* conditions resemble well those of Ni_xB-300 measured *ex-situ*, showing the presence of both $Ni(OH)_2$ structure (peaks at 1.55 and 2.73 Å corresponding to Ni-O and Ni-Ni^{2+} backscattering), and Ni-B in the first coordination sphere represented by a small peak at 2.15 Å (all uncorrected for a phase shift). The fitted Ni-O distance does not change after the electrochemical cycling pre-treatment as compared to the untreated sample, but reduces first to 2.05 Å at 1.0 V and then to 2.03 Å at 1.7 V (see Table S4). At the same time, the corresponding coordination numbers decrease from 3.7 to 3.3 and 3.0 for the pre-conditioned sample, and during polarization at 1.0 V and at 1.7 V, respectively. The Ni-Ni^{2+} coordination number changes drastically from 5.7 to 4.0 when comparing the prepared sample to that measured under operando conditions at 1.7 V. The changes observed in the EXAFS features,

associated with the Ni^{2+} state can have twofold explanation. Firstly, the significant change of coordination number in the Ni-Ni^{2+} backscattering pair compared to Ni-O points to a less ordered structure under harsh OER conditions since the more distant coordination shells are more sensitive to a material's long range order. Another explanation is associated with the chemical state changes observed on the XANES spectra. Both $Ni(OH)_2$ and NiOOH structures form Ni-O as well as Ni-Ni^{X+} (X = 2, 3) backscattering signals, however shifted by ca. 0.3 Å towards shorter distances in the case of Ni^{3+}. When both structures are present in the sample, the corresponding photoelectron waves interfere destructively due to phase mismatch. This hypothesis is supported by the apparent contraction of the Ni-O bond observed at 1.7 V_{RHE}, consistent with observations by other groups[36,37].

In the abridged mechanism of O_2 evolution,[38,39] involving the reaction sequence: (i) $M + OH^- \rightarrow MOH + e^-$; (ii) $MOH + OH^- \rightarrow MO + H_2O + e^-$; (iii) $MO + OH^- \rightarrow MOOH + e^-$; (iv) $MOOH + OH^- \rightarrow MO_2 + H_2O + e^-$; and (v) $MO_2 \rightarrow M + O_2$, equations (i) to (iii) all involve growth of an oxide layer. In (i) and (ii), Ni is present as Ni^{2+}, while (iii) involves Ni^{2+} to Ni^{3+} transition, and in (iv) Ni^{3+} is oxidized to Ni^{4+}. Based on this mechanism, a fingerprint of Ni^{4+} should be trackable under active oxygen evolution conditions using a suitable *operando* technique[36]. By employing *pseudo-operando* XAFS, and other complementary *in-situ* techniques to track the redox states of Ni and Fe in a Ni-Fe(OOH) catalyst, Strasser et al.[36,40], observed that, for a low content of Fe in the catalyst, < 4%, Ni^{4+} was the dominant redox state of Ni under catalytic OER conditions. Conversely, a high Fe content, > 4%, stabilized the Ni^{2+} state thereby suppressing the higher-valent states of Ni (Ni^{3+} and Ni^{4+}) under catalytic O_2 evolution conditions, resulting in faster oxygen evolution kinetics at the expense of the oxidation of Ni^{2+}. The authors concluded based on these observations, that $Ni^{2+}Fe^{3+}OOH$, is the active state of the Ni-Fe(OOH) catalyst under catalytic conditions. For bulk electrode materials, the OER takes place on a thin surface oxide-hydroxide layer making it challenging to observe the transient states of OER catalysts whose bulk properties predominate the surface properties by employing an averaging technique. The Ni_xB-300 catalyst probed here comprised of ultrathin sheets of atomic scale thickness (≈ 6.6 Å), with a core-shell (Ni-B@NiO_x) structure, where the surface properties (Ni^{2+}) predominated the core properties (Ni-B), as demonstrated by XAFS in Fig. 3, which makes the catalyst suitable for *operando* XAFS studies. Our *operando* XAFS studies did not disclose any features attributable to the Ni^{4+} state at active O_2 evolution potentials. To

rationalize this observation on the premise of the mechanism outlined above, deoxygenation of the NiO_2 intermediate, step (v) has to be comparatively faster in relation to the other reaction steps. Interestingly, our observations lead to a conclusion which appears to be coherent with the work of Strasser et al.[36,40]. Our findings there present new insights into the dynamics of OER catalyst structures under reaction conditions, as well as the dynamics of some transient states of the catalyst during the OER.

Conclusions

Nickel boride (Ni_xB) comprised of very thin sheets and small nanoparticles with a Ni-B core and nickel hydroxide shell (Ni-B@$Ni(OH)_2$) structure is unveiled as a highly efficient and stable electrocatalyst for oxygen evolution under alkaline conditions. When supported on nickel foam, the catalyst drives the OER at 20 mA cm^{-2} at only 0.28 V overpotential in 1.0 M KOH. We observed by operando XAFS, intactness of the Ni-B core under active oxygen evolution, and simultaneously, a transition of Ni^{2+} to Ni^{3+} (NiOOH) in the shell leading to shortening of Ni-O bonds and increase in disorder of the nickel oxyhydroxide layer. The synthesis of nickel boride is simple and readily scalable, making it a very attractive and competitive non-precious anode catalyst in ECWS for mass hydrogen production.

References

1. Barbir, F. PEM electrolysis for production of hydrogen from renewable energy sources. *Solar Energy* **78,** 661–669 (2005).
2. Zeng, K. & Zhang, D. Recent progress in alkaline water electrolysis for hydrogen production and applications. *Prog. Energ. Combust* **36,** 307–326 (2010).
3. Reier, T., Oezaslan, M. & Strasser, P. Electrocatalytic Oxygen Evolution Reaction (OER) on Ru, Ir, and Pt Catalysts: A Comparative Study of Nanoparticles and Bulk Materials. *ACS Catal.* **2,** 1765–1772 (2012).
4. Lee, Y., Suntivich, J., May, K. J., Perry, E. E. & Shao-Horn, Y. Synthesis and Activities of Rutile IrO 2 and RuO 2 Nanoparticles for Oxygen Evolution in Acid and Alkaline Solutions. *J. Phys. Chem. Lett,* 399–404 (2012).
5. Han, L., Dong, S. & Wang, E. Transition-Metal (Co, Ni, and Fe)-Based Electrocatalysts for the Water Oxidation Reaction. *Adv. Mater.* **28,** 9266–9291 (2016).

6. Anantharaj, S. *et al.* Recent Trends and Perspectives in Electrochemical Water Splitting with an Emphasis on Sulfide, Selenide, and Phosphide Catalysts of Fe, Co, and Ni. A Review. *ACS Catal.* **6,** 8069–8097 (2016).

7. Enman, L. J., Burke, M. S., Batchellor, A. S. & Boettcher, S. W. Effects of Intentionally Incorporated Metal Cations on the Oxygen Evolution Electrocatalytic Activity of Nickel (Oxy)hydroxide in Alkaline Media. *ACS Catal.* **6,** 2416–2423 (2016).

8. Burke, M. S., Kast, M. G., Trotochaud, L., Smith, A. M. & Boettcher, S. W. Cobalt-iron (oxy)hydroxide oxygen evolution electrocatalysts: the role of structure and composition on activity, stability, and mechanism. *J. Am. Chem. Soc.* **137,** 3638–3648 (2015).

9. Lu, X. & Zhao, C. Electrodeposition of hierarchically structured three-dimensional nickel-iron electrodes for efficient oxygen evolution at high current densities. *Nat Comms* **6,** 6616 (2015).

10. Gong, M. *et al.* An advanced Ni-Fe layered double hydroxide electrocatalyst for water oxidation. *J. Am. Chem. Soc.* **135,** 8452–8455 (2013).

11. Song, F. & Hu, X. Exfoliation of layered double hydroxides for enhanced oxygen evolution catalysis. *Nat Comms* **5,** 4477 (2014).

12. Masa, J. *et al.* Low Overpotential Water Splitting Using Cobalt–Cobalt Phosphide Nanoparticles Supported on Nickel Foam. *ACS Energy Lett.* **1,** 1192–1198 (2016).

13. Popczun, E. J. *et al.* Nanostructured Nickel Phosphide as an Electrocatalyst for the Hydrogen Evolution Reaction. *J. Am. Chem. Soc.* **135,** 9267–9270 (2013).

14. Popczun, E. J., Read, C. G., Roske, C. W., Lewis, N. S. & Schaak, R. E. Highly Active Electrocatalysis of the Hydrogen Evolution Reaction by Cobalt Phosphide Nanoparticles. *Angew. Chem. Int. Ed.* **53,** 5427–5430 (2014).

15. Long, X. *et al.* Metallic Iron-Nickel Sulfide Ultrathin Nanosheets As a Highly Active Electrocatalyst for Hydrogen Evolution Reaction in Acidic Media. *J. Am. Chem. Soc.* **137,** 11900–11903 (2015).

16. Zhu, W. *et al.* Nickel sulfide microsphere film on Ni foam as an efficient bifunctional electrocatalyst for overall water splitting. *Chem. Commun* **52,** 1486–1489 (2016).

17. Zhou, H. *et al.* Efficient hydrogen evolution by ternary molybdenum sulfoselenide particles on self-standing porous nickel diselenide foam. *Nat Comms* **7,** 12765 (2016).

18. Vrubel, H. & Hu, X. Molybdenum Boride and Carbide Catalyze Hydrogen Evolution in both Acidic and Basic Solutions. *Angew. Chem. Int. Ed.* **124,** 12875–12878 (2012).

19. Glavee, G. N., Klabunde, K. J., Sorensen, C. M. & Hadjapanayis, G. C. Borohydride reductions of metal ions. A new understanding of the chemistry leading to nanoscale particles of metals, borides, and metal borates. *Langmuir* **8,** 771–773 (1992).

20. Blanchard, P. E. R., Grosvenor, A. P., Cavell, R. G. & Mar, A. X-ray Photoelectron and Absorption Spectroscopy of Metal-Rich Phosphides M_2P and M_3P (M = Cr−Ni). *Chem. Mater.* **20,** 7081–7088 (2008).

21. Schreifels, J. X-Ray photoelectron spectroscopy of nickel boride catalysts: Correlation of surface states with reaction products in the hydrogenation of acrylonitrile. *J. Catal.* **65,** 195–206 (1980).

22. Carenco, S., Portehault, D., Boissière, C., Mézailles, N. & Sanchez, C. Nanoscaled metal borides and phosphides: recent developments and perspectives. *Chem. Rev.* **113,** 7981–8065 (2013).

23. Demirci, U. B. & Miele, P. Cobalt in NaBH4 hydrolysis. *Phys. Chem. Chem. Phys.* **12,** 14651–14665 (2010).

24. Arzac, G. M., Rojas, T. C. & Fernández, A. New insights into the synergistic effect in bimetallic-boron catalysts for hydrogen generation: The Co–Ru–B system as a case study. *Appl. Catal., B* **128,** 39–47 (2012).

25. Shveikin, G. P. & Ivanovskii, A. L. The chemical bonding and electronic properties of metal borides. *Russ. Chem. Rev.* **63,** 711–734 (1994).

26. Tang, C., Cheng, N., Pu, Z., Xing, W. & Sun, X. NiSe Nanowire Film Supported on Nickel Foam: An Efficient and Stable 3D Bifunctional Electrode for Full Water Splitting. *Angew. Chem. Int. Ed.* **54,** 9351–9355 (2015).

27. Ledendecker, M. *et al.* The Synthesis of Nanostructured Ni5 P4 Films and their Use as a Non-Noble Bifunctional Electrocatalyst for Full Water Splitting. *Angew. Chem. Int. Ed.* (2015).

28. Stern, L.-A., Feng, L., Song, F. & Hu, X. Ni 2 P as a Janus catalyst for water splitting. The oxygen evolution activity of Ni_2P nanoparticles. *Energy Environ. Sci.* **8,** 2347–2351 (2015).

29. Shalom, M. *et al.* Nickel nitride as an efficient electrocatalyst for water splitting. *J. Mater. Chem. A* **3,** 8171–8177 (2015).

30. Zhu, Y.-P., Liu, Y.-P., Ren, T.-Z. & Yuan, Z.-Y. Self-Supported Cobalt Phosphide Mesoporous Nanorod Arrays. A Flexible and Bifunctional Electrode for Highly Active Electrocatalytic Water Reduction and Oxidation. *Adv. Funct. Mater,* **25** 7337–7347 (2015).

31. Zhou, W. *et al.* Ni_3S_2 nanorods/Ni foam composite electrode with low overpotential for electrocatalytic oxygen evolution. *Energy Environ. Sci.* **6,** 2921–2924 (2013).

32. Maljusch, A., Conradi, O., Hoch, S., Blug, M. & Schuhmann, W. Advanced Evaluation of the Long-Term Stability of Oxygen Evolution Electrocatalysts. *Anal. Chem* **88,** 7597–7602 (2016).

33. Chen, S. *et al.* Three-Dimensional Smart Catalyst Electrode for Oxygen Evolution Reaction. *Adv. Energy Mater.* **5,** 1500936 (2015).

34. Gul, S. *et al.* Simultaneous detection of electronic structure changes from two elements of a bifunctional catalyst using wavelength-dispersive X-ray emission spectroscopy and in situ electrochemistry. *Phys. Chem. Chem. Phys.* **17,** 8901–8912 (2015).

35. Mansour, A. N. X-Ray Absorption Fine Structure Spectra and the Oxidation State of Nickel in Some of Its Oxycompounds. *J. Electrochem. Soc.* **141,** L69-L71 (1994).

36. Gorlin, M. *et al.* Oxygen Evolution Reaction Dynamics, Faradaic Charge Efficiency, and the Active Metal Redox States of Ni-Fe Oxide Water Splitting Electrocatalysts. *J. Am. Chem. Soc.* **138,** 5603–5614 (2016).

37. Dionigi, F. & Strasser, P. NiFe-Based (Oxy)hydroxide Catalysts for Oxygen Evolution Reaction in Non-Acidic Electrolytes. *Adv. Energy Mater.* **6,** 1600621 (2016).

38. Matsumoto, Y. & Sato, E. Electrocatalytic properties of transition metal oxides for oxygen evolution reaction. *Mater. Chem. Phys.* **14,** 397–426 (1986).

39. Dau, H. *et al.* The Mechanism of Water Oxidation. From Electrolysis via Homogeneous to Biological Catalysis. *ChemCatChem* **2,** 724–761 (2010).

40. Goerlin, M. *et al.* Tracking catalyst redox states and reaction dynamics in Ni-Fe oxyhydroxide oxygen evolution reaction (OER) electrocatalysts: The role of catalyst support and electrolyte pH. *J. Am. Chem. Soc.* (2017). DOI: 10.1021/jacs.6b12250

Acknowledgements

The authors are grateful to Mr. Daniel Peters for support with XRD measurements and interpretation, Dr. Wei Xia and Dr. Christoph Somsen for TEM analysis and interpretation, and Ms. Sandra Schmidt for SEM measurements. Staff of beamlines 2-2 (Stanford Synchrotron Radiation Lightsource), ID10 (Advanced Photon Source) and SAMBA (SOLEIL) are acknowledged for their support during XAFS measurements. This work was made possible thanks to the financial support from the US National Science Foundation (NSF-Chemistry 1213182) and the Cluster of Excellence RESOLV at RUB (EXC 1069) funded by the Deutsche Forschungsgemeinschaft. BRC and IS gratefully acknowledges financial support from the U.S. National Science Foundation (NSF-Chemistry 1213182) and the German Federal Ministry of Education and Research (Bundesministerium fuer Bildung und Forschung, BMBF) under grant #03SF0523C, CO2EKAT and the Cluster of Excellence RESOLV at RUB (EXC 1069) funded by the Deutsche Forschungsgemeinschaft. MdlM, AG and JA acknowledge funding from Generalitat de Catalunya 2014 SGR 1638 and the Spanish MINECO coordinated projects between IREC and ICN2 TNT-FUELS and e-TNT and ICN2 Severo Ochoa Excellence Program.

Author Contribution

JM and WS conceived the idea, planned the experiments and wrote the manuscript, IS, HM and BRC performed XAFS measurements, designed cells for operando XAS measurements, discussed and interpreted XAFS data and participated in writing parts of the manuscript, EV contributed in electrochemical experiments, discussion and data interpretation, MdlM, and JA did the (S)TEM and EELS measurements and helped with interpretation of crystallographic data, IS and MM contributed with the XPS measurements, discussions and data interpretation.

Author Information

Correspondence and requests for materials should be addressed to justus.masa@rub.de and wolfgang.schuhmann@rub.de

Additional information

Supplementary information, reprints and permissions information is available online at www.nature.com/reprints. Correspondence and requests for materials should be addressed to J.M. and W.S.

Competing financial interests

The authors declare no competing financial interests.

Table of contents (TOC) image